Journal of Geophysical Research: Atmospheres

RESEARCH ARTICLE
10.1029/2018JD028940

Sea Breeze Sensitivity to Coastal Upwelling and Synoptic Flow Using Lagrangian Methods

Greg Seroka[1,2], Erick Fredj[3], Josh Kohut[1], Rich Dunk[1], Travis Miles[1], and Scott Glenn[1]

[1]Center for Ocean Observing Leadership, Department of Marine and Coastal Sciences, Rutgers, The State University of New Jersey, New Brunswick, NJ, USA, [2]Now at Coast Survey Development Laboratory, Office of Coast Survey, National Ocean Service, NOAA, Silver Spring, MD, USA, [3]Department of Computer Sciences, Jerusalem College of Technology, Jerusalem, Israel

Key Points:
- Lagrangian method applied to weather model reveals synoptic flow impacts sea breeze onshore extent more than offshore in U.S. Mid-Atlantic
- Upwelling did not greatly impact sea breeze onshore/offshore extent, but produced earlier, shallower, sharper, and stronger sea breeze
- Results agree with sea breeze theory, proving utility of Lagrangian methods for sea breeze prediction, offshore wind resource assessment

Correspondence to:
G. Seroka,
gregory.seroka@noaa.gov

Citation:
Seroka, G., Fredj, E., Kohut, J., Dunk, R., Miles, T., & Glenn, S. (2018). Sea breeze sensitivity to coastal upwelling and synoptic flow using Lagrangian methods. *Journal of Geophysical Research: Atmospheres*, *123*, 9443–9461. https://doi.org/10.1029/2018JD028940

Received 2 MAY 2018
Accepted 20 AUG 2018
Accepted article online 30 AUG 2018
Published online 12 SEP 2018

Abstract Sea breezes occur nearly daily in the U.S. Mid-Atlantic summer during high electricity demand periods, and thus have important implications for the burgeoning U.S. offshore wind energy industry. The sea breeze's offshore component is poorly understood and ill defined relative to its onshore counterpart. Here a new Lagrangian method not yet readily used to study the sea breeze, relative dispersion, was validated and applied to a validated Weather Research and Forecasting model in the U.S. Mid-Atlantic. This Lagrangian method is used to characterize the onshore convergent and offshore divergent sea breeze extents and intensities, and test their sensitivities to both atmospheric synoptic flow and oceanic coastal upwelling, another common summer season regional phenomenon. It was found that offshore-directed synoptic flow impacted the sea breeze onshore extent more than offshore extent, and that coastal upwelling did not significantly impact sea breeze onshore or offshore extent for these carefully selected case studies. Upwelling, however, produced an earlier sea breeze onset (~5 hr), and a shallower, sharper, and more intense offshore/onshore sea breeze during strong offshore synoptic flow, consistent with past studies. The offshore side of the sea breeze cell—with stronger intensity during upwelling—crossed the New Jersey Wind Energy Area at ~1900 UTC, regardless of synoptic wind or upwelling conditions. Results overall are consistent with dynamic linear sea breeze theory. Uncertain projected trends in coastal upwelling/sea breezes in a warming world highlight the importance of continued study of coastal air-sea interactions for improved offshore wind energy assessment and prediction.

Plain Language Summary Sea breezes are important for the emerging U.S. offshore wind energy industry, because they occur frequently during peak energy demand periods (summer afternoons) across many of the nation's coastlines designated for offshore wind energy. However, the offshore component of the sea breeze—where offshore wind turbines operate—is poorly understood. Here a Lagrangian analysis technique called relative dispersion is newly applied to a numerical weather prediction model in the U.S. Mid-Atlantic. The new technique enables clearer characterization of the offshore sea breeze component. It was found that winds against the sea breeze prevented the sea breeze from penetrating inland, whereas those same winds largely did not affect the offshore extent of the sea breeze. When coastal upwelling occurred—resulting in very cold waters at the beach, the sea breeze began ~5 hr earlier and was stronger. Regardless of the condition tested, the offshore extent of the sea breeze crossed the New Jersey Wind Energy Area at ~1900 UTC. The results here are consistent with past studies and sea breeze theory. The new application of the technique should be a useful tool for further characterization and prediction of the sea breeze offshore, which will be critical for offshore wind energy applications.

1. Introduction

The sea breeze circulation, caused by the thermal contrast between the land and sea, has been well documented since at least ancient Greece (Steele et al., 2013), especially over land. In general, over land observations are more prevalent than observations over the coastal ocean. Consequently, there have been many onshore implications and studies of the sea breeze, ranging from coastal/inland air quality (Pielke, 1991; Ratcliff et al., 1996) including low-level ozone (Lalas et al., 1983), forest fires (Rothermel, 1983), nuclear power plant concerns (Venkatesan et al., 2002), beach recreation (De Freitas, 1990), and heat waves (Papanastasiou et al., 2010). The offshore component of the sea breeze, in contrast, has received less attention due to the

relative paucity of observations. Offshore sea breeze studies have thus been mostly restricted to numerical simulations (e.g., Steele et al., 2014, and references within).

In recent years, interest in offshore wind energy in the United States has increased, with the country's first offshore wind farm becoming operational offshore of Block Island, RI, in late 2016. Therefore, in the United States, where this study takes place, the offshore component of the sea breeze has thus gained wider significance within the country for not only the sailing and fishing communities but now also for the offshore wind energy industry. Of course, with offshore wind energy generation existing in Europe for nearly three decades and China for nearly a decade, the sea breeze's significance to offshore energy in those regions has and will continue to remain high.

Unlike the onshore side of the sea breeze where the inland frontal boundary is clearly defined and visible on weather radar by a distinct front, the offshore side and its spatial scales are much more difficult to distinguish and define objectively (Finkele, 1998). One definition that has been used is the cutoff of 1.0-m/s onshore wind speed within the lowest 100 m of the sea breeze circulation (Arritt, 1989). However, this can only be applied in offshore synoptic wind conditions. Alternatively, the offshore extent can be defined as the point where the wind speed is uninfluenced by the sea breeze, which greatly increases the distance to the offshore boundary. In the "convectional" theory of the sea breeze (Rotunno, 1983), the extensive calm region near the Earth's surface that frequently occurs near this point—highly dependent on synoptic wind direction and speed—does not necessarily represent the region of largest surface divergence. This is in contrast to the onshore front that represents the region of largest surface convergence for the vast majority of sea breeze types and intensities.

Accordingly, new methods to study the ill-defined and less-studied offshore side of the sea breeze are needed to fully understand its impact on the offshore wind energy resource. Here we apply Lagrangian methods (Haller, 2015) to map the offshore extent of the sea breeze cell and to quantify the sensitivity of sea breeze features to varying oceanic and atmospheric conditions. Relative dispersion (RD) is a statistical quantity used in the description of Lagrangian coherent structures (LCSs), which are boundaries in a fluid that distinguish regions of differing dynamics within the Lagrangian point of view, which is frame independent (Haller, 2015). The Lagrangian RD approach identifies regions that play a dominant role in attracting and repelling neighboring elements in a fluid flow (in our case, the sea breeze circulation) over a selected period of time. An important consideration that needs to be mentioned in this study of flow barriers in time is that features such as trenches or ridges of the RD at different times do not advect into each other. For example, an RD ridge at time t_1 does not necessarily advect into an RD ridge at time t_2, so there can be a significant material flux across these structures. Nevertheless, as will be shown, RD in its Lagrangian framework provides some new clarity in identification of sea breeze features both onshore and offshore.

Again, in the convectional theory of the sea breeze, one would expect onshore convergence, rising air, and an attracting RD region near the Earth's surface defining the inland extent, and offshore divergence, sinking air, and a repelling RD region defining the offshore extent. In this framework, the previously ill-defined offshore extent can be quantified in any synoptic flow conditions. Further, RD in conjunction with atmospheric modeling of the sea breeze allows for objective sensitivities of the offshore extent and intensity of the sea breeze to forcings like synoptic flow strength and land-sea thermal contrast—that is, coastal upwelling presence versus absence, described next.

The Mid-Atlantic Bight (MAB) off the U.S. East Coast is an ideal sea breeze test bed due to frequent sea breeze and coastal upwelling interactions in a region of forthcoming offshore wind energy development. During the spring season, the ocean across the entire MAB continental shelf is well mixed and cold from the previous winter (Figure 1a; Bigelow, 1933). The thermal contrast between the cold coastal ocean and warming land surfaces in the spring leads to numerous sea breezes. During the summer, the MAB becomes a two-layer stratified ocean (e.g., Castelao et al., 2008) with warm surface waters approaching 26 °C heated by solar radiation, and cold bottom water—the MAB Cold Pool—remaining 8 °C or lower from the previous winter and spring (as in Figure 1a) and replenished by southwestward advection of northern cold water (Houghton et al., 1982). Although the surface waters are warming throughout the spring, the land surfaces are warming at a much greater rate, leading to sufficient thermal contrasts for frequent afternoon sea breezes over the coastal U.S. Mid-Atlantic. During the MAB summer, coastal upwelling can also occur frequently. Seasonal synoptic winds from the southwest, flowing around the prominent summertime Bermuda High, drive a surface ocean Ekman

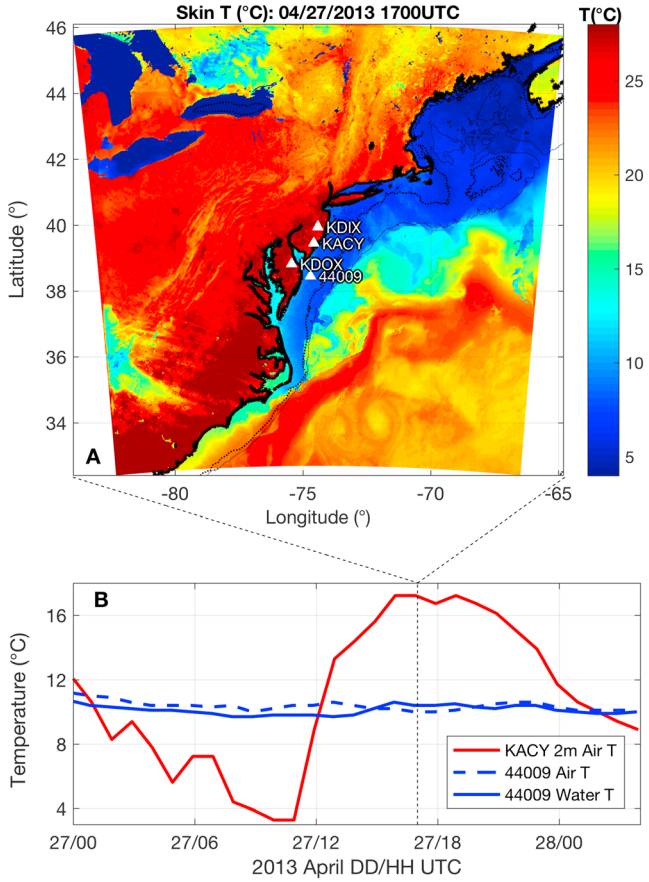

Figure 1. 27 April 2013. (a) WRF skin temperature (°C) at 1700 UTC on 27 April 2013, showing the entire WRF domain. White triangles mark KACY airport, KDIX and KDOX weather radar, and NDBC buoy 44009 locations; the thick dotted black contour is the 50-m isobath; and the thin dotted black contour is the 200-m isobath. (b) Time series of KACY 2mT, 44009 air temperature, and 44009 water temperature (°C), with vertical dotted line marking time of WRF skin temperature map above.

transport offshore. The cold pool of water along the bottom of the MAB is consequently advected toward the coast and upwells along the beach (Figure 2; e.g., Glenn et al., 2004).

A mean coastal upwelling sea surface temperature (SST) signal for the MAB shows a recurrent upwelling center south of Long Island, three recurrent centers along the New Jersey (NJ) coast, and one farther south off the northern Delmarva coast (Figure 2a). The recurrent centers along NJ have been noted to occur downstream of a series of bathymetric highs associated with ancient river deltas (Glenn et al., 1996, 2004). The maximum extent of coastal upwelling during the three-year time period chosen is also shown (Figure 2b), with filaments of upwelling extending through the New Jersey Wind Energy Area (NJ WEA)—designated for offshore wind energy development—and out to almost the shelf break at ~200 m. Another example of coastal upwelling from the 2012–2014 time period is depicted in Figure 3b.

Coastal upwelling not only has large spatial extent across the MAB, but its occurrence also has large temporal extent throughout the MAB sea breeze season and during the summer peak energy demand period. Three-year mean daily max load data from the Mid-Atlantic Region of the Pennsylvania-New Jersey-Maryland interconnection are paired with monthly frequency of NJ sea breeze days and coastal upwelling days (Figure 4). The results show that the seasonal peaks in sea breeze and coastal upwelling are both coincident with the seasonal peak in electricity demand in the region (Figure 4). The spring and summer peaks in sea breeze days are also apparent, as is the summer to early fall peak in upwelling days. This graph reiterates that a more complete understanding of the impact of coastal upwelling on the offshore component of the MAB sea breeze circulation is critical for a comprehensive offshore wind resource assessment during important peak energy demand periods.

In addition to studying the influence of coastal upwelling on the sea breeze, we also test the circulation's sensitivity to different synoptic flow strengths. It has been previously found in Australia that the offshore extent of the sea breeze is less sensitive to offshore synoptic wind than its inland extent (Finkele, 1998). We test this result for the U.S. MAB, across varying offshore synoptic wind strengths.

This study integrates validated numerical modeling techniques (Weather Research and Forecasting (WRF)) of the sea breeze, high-resolution satellite SST composites designed to capture and not remove coastal upwelling, weather radar observations of the inland sea breeze front, and a Lagrangian method to objectively define the onshore/offshore extent and intensity of the MAB sea breeze. Using these techniques, this paper will investigate the sensitivity of the offshore and onshore MAB sea breeze circulation components to atmospheric (synoptic flow) and oceanic (coastal upwelling) forcing, and compare the end results to dynamic linear sea breeze theory.

2. Data and Methods

2.1. Sea Breeze Types for NJ

The sea breeze can be classified into four main types based on synoptic winds. These include, for the Northern Hemisphere, (a) *pure*, when the largest synoptic wind component is perpendicular to the coast and in the offshore direction, opposing the sea breeze flow; (b) *corkscrew*, when the largest synoptic wind component is parallel to the coast with the land surface to the left; (c) *backdoor*, when the largest synoptic wind component is parallel to the coast with the land surface to the right; and (d) *synoptic*, when any wind —sea breeze or synoptic—is blowing onshore from sea to land and enhancing the near surface sea breeze

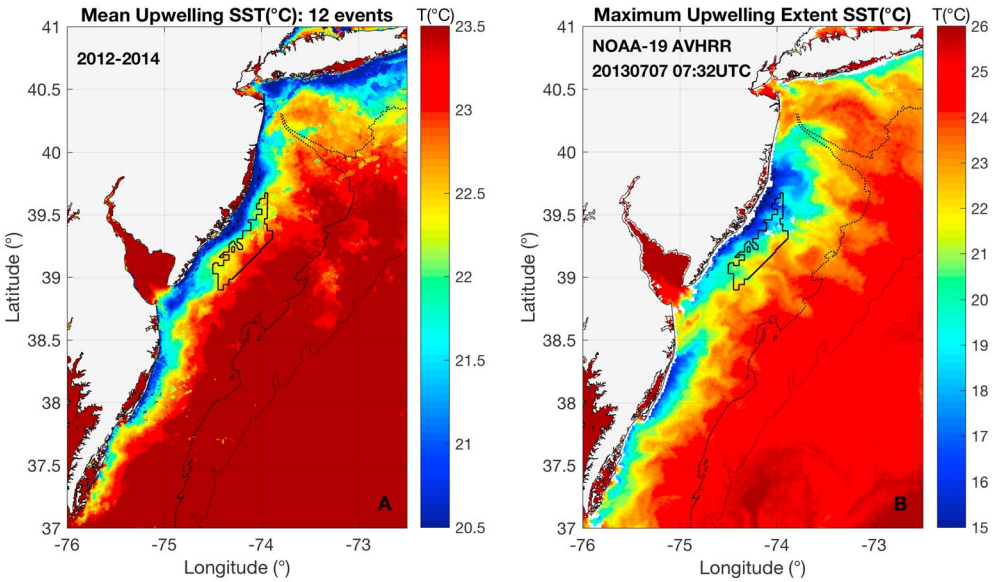

Figure 2. (a) The average SST (°C) across one representative AVHRR scan for each of the 12 upwelling events that occurred 2012–2014. NJ WEA plotted in the black boxed contour SE of NJ, thick dotted black contour is the 50-m isobath, and thin dotted black contour is the 200-m isobath. (b) Same as in (a) but for maximum upwelling extent SST (°C) during the 2012–2014 period.

winds (Miller et al., 2003). See Miller et al. (2003) and Steele et al. (2014) for graphical depictions of these main sea breeze classifications.

In spring 2002–2007 over the MAB, dominant surface wind direction was from the SSW (~32% of the time), with secondary peaks in wind direction from the NW (21%) and NE (21%). In summer 2002–2007, dominant surface wind direction was again from the SSW (48%), with secondary peaks from the NE (15%) and NW (11%; Gong et al., 2010). This wind climatology suggests that during the spring and summer in the six-year period, the dominant sea breeze type for NJ would likely have been *corkscrew*, with *pure* and *backdoor* secondary and *synoptic* the least likely to occur.

2.2. Environmental Data

National Data Buoy Center (NDBC) buoys 44009 and 44065 provided surface meteorology and ocean conditions. For both spring and summer sea breeze cases (described in section 2.5), water temperature from 44009 at 0.6-m depth was used. For the spring case, air temperature from 44009 at 4-m height was used. For the summer case, air temperature from 44065 at 4-m height was used, as air temperature from 44009 was not available. Atlantic City International Airport (KACY) provided hourly 2-m air temperature (2mT) data, which were used in conjunction with the surface air and water temperature data from the NDBC buoys to depict land-sea thermal contrasts in Figures 1 and 3.

U.S. Coastal Relief Model data from the NOAA National Centers for Environmental Information were used for water depth and coastlines throughout (NOAA National Geophysical Data Center, 1999).

The empirically derived declouding techniques specific for the MAB and described in Glenn et al. (2016) were used to remove bright cloud covered pixels from daytime advanced very high resolution radiometer data while retaining the darker ocean pixels. These individual declouded advanced very high resolution radiometer passes were used to create the mean and maximum upwelling extents in Figure 2. The same three-day "coldest dark pixel" SST compositing technique described in Glenn et al. (2016) was used to map and preserve cold coastal upwelling regions. These SST composites were used as bottom boundary conditions over water for WRF simulations (Figures 1 and 3; described in more detail below).

Next-Generation Radar (NEXRAD) clear-air mode level-II data (NOAA National Centers for Environmental Information, 2017) from KDIX (New Jersey) and KDOX (Delaware) were used for inland sea breeze front identification. Dust and insects can be collected within the inland sea breeze frontal convergence zone,

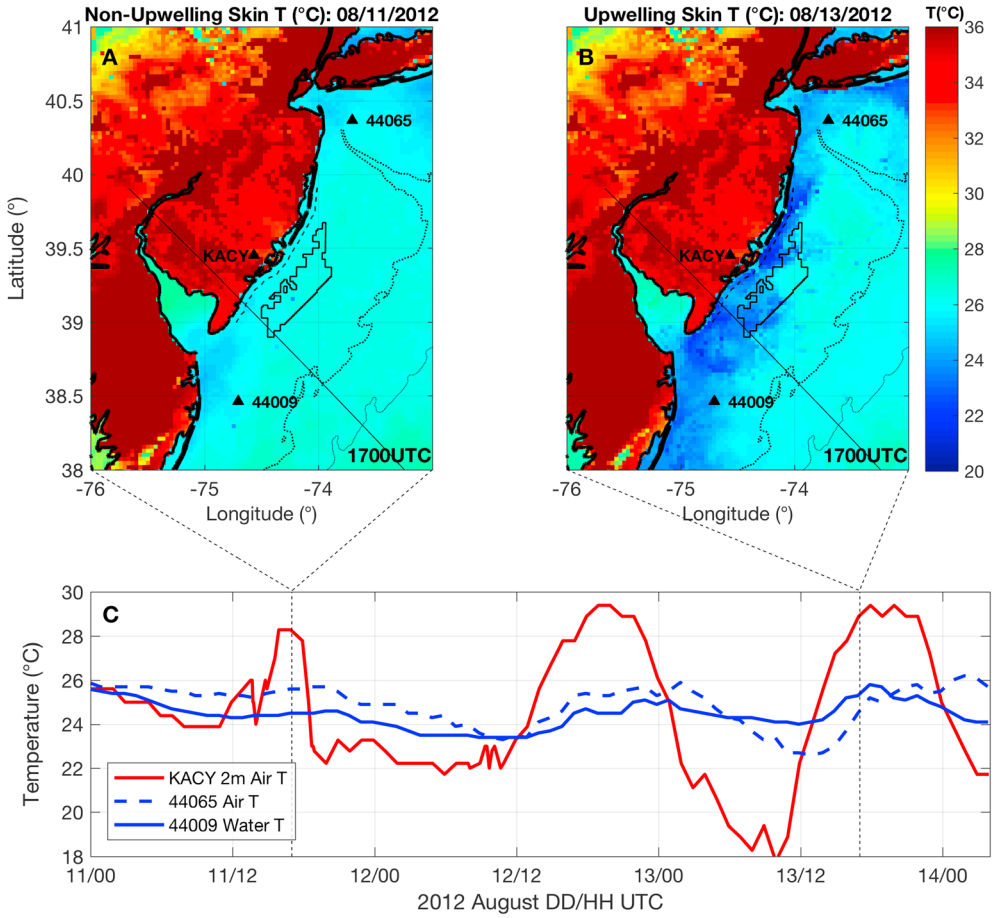

Figure 3. 13 August 2012. Same as in Figure 1 but for the 13 August 2012 upwelling case, (a) with nonupwelling WRF skin temperature (°C) (b) two days prior to the upwelling WRF skin temperature. NDBC buoys 44065, 44009, and KACY marked as black triangles. Dashed line near NJ coast in (a) and (b) marks state/federal waters boundary, and NW to SE line marks NJ cross-section location.

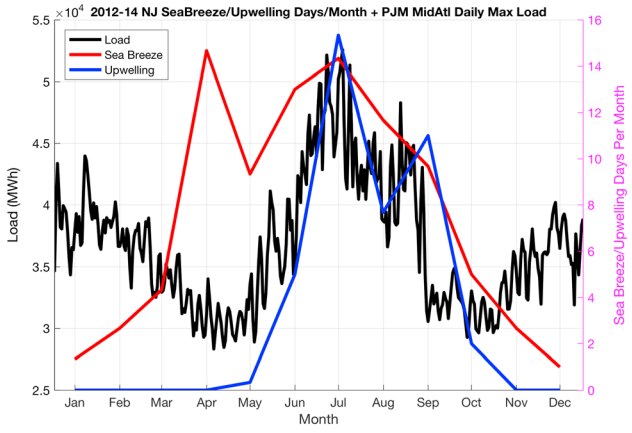

Figure 4. 2012–2014. Averaged PJM Mid-Atlantic region daily maximum load (black; MWh), 2012–2014 NJ sea breeze (red) and upwelling (blue) average days per month. Sea breeze (upwelling) days were counted if the weather radar (satellite SST) imagery for that day contained a clear visual of the sea breeze front (cold upwelled water); the three-year average was then calculated by dividing the monthly count first by 3 (for 3 years) and then by the number of days in the month.

producing high reflectivity in the weather radar return (Atlas, 1960). Base elevation scans were used in Figures 6 and 8, for observational verification of the RD identification of the inland sea breeze front.

2.3. WRF

WRF-ARW version 3.6.1 was used for this study. The 3-km resolution WRF-ARW domain is depicted in Figure 1. The North American Mesoscale 12-km model was used for initial conditions and lateral boundary conditions. The coldest dark pixel SST composites described above were used for bottom boundary conditions over the ocean. Our model setup included longwave radiation physics computed by the Rapid Radiative Transfer Model, shortwave radiation physics computed by the Dudhia scheme, the MM5 Monin-Obukhov atmospheric layer model and the Noah land surface model used with the Yonsei University planetary boundary layer (PBL) scheme (consistent with Steele et al., 2014), and the WRF single-moment class-3 moisture microphysics scheme (Hong et al., 2004) used for grid-scale precipitation processes. WRF output was set for every 10 min and simulations were initialized at 00*Z* on the day of the sea breeze.

Given that the offshore sea breeze extent has been found to be sensitive to PBL scheme (Steele et al., 2014), we tested model sensitivity to PBL scheme on the spring sea breeze case, comparing Yonsei University to Mellor-Yamada-Nakanishi-Niino PBL scheme (Nakanishi & Niino, 2004, 2006). Mellor-Yamada-Nakanishi-Niino PBL scheme has been found to be the best PBL scheme for the offshore environment (Munoz-Esparza & Canadillas, 2012), while Yonsei University has been used in a previous offshore sea breeze climatology study for the UK (Steele et al., 2014). Results of this comparison show that both inland and offshore extents are not sensitive to choice of PBL scheme.

A similar WRF configuration (Rutgers University-WRF) used for NJ offshore wind energy applications was validated against coastal and offshore monitoring systems using criteria accepted by the wind energy industry and the National Renewable Energy Laboratory's National Wind Technology Center for determining model performance (Dvorak et al., 2013). These criteria include comparisons between (1) standard deviation (STD) of the model (σ_{model}) and STD of the observations (σ_{obs}; criterion is $\sigma_{model} \sim = \sigma_{obs}$), (2) root-mean-square error of the model (RMSE) and σ_{obs} (criterion is RMSE $< \sigma_{obs}$), and (3) an unbiased version of RMSE ($RMSE_{ub}$) and σ_{obs} (criterion is $RMSE_{ub} < \sigma_{obs}$). Results show that the model is validated and can be used to analyze and predict NJ's coastal/offshore wind resource (Dunk & Glenn, 2013). Further, validation was performed of the WRF-simulated offshore wind conditions in the cases selected for this study. This validation compared observed and WRF-simulated wind speed and direction at NDBC buoy 44009; results show good agreement between model and observations.

2.4. Lagrangian Methods

LCS metrics (Gildor et al., 2009; Haller, 2015; Haller & Yuan, 2000) were used to characterize the onshore and offshore boundaries of the sea breeze circulation. Conventional divergence or subsidence fields of the WRF winds would produce a low signal-to-noise ratio, but by using the Lagrangian framework we are able to increase the signal-to-noise ratio (Tang et al., 2011b) to produce a more effective sea breeze boundary clarification, especially in the traditionally difficult-to-define offshore zone. Past studies, including Tang et al. (2011a, 2011b), have validated and proven the value of Lagrangian methods to analyze turbulent wind patterns near airports, including offshore.

First, particles were placed on a 10-km resolution grid within the 3-km WRF wind fields. Then, the particles were advected within each horizontal layer by the horizontal components of the winds every 10 min over 1 hr—that is, independent forward trajectories—at various levels throughout the marine atmospheric boundary layer. These 1-hr short trajectory "simulations" were performed for 1700–1800, 1800–1900, 1900–2000, 2000–2100, 2100–2200, 2200–2300, and 2300–0000 UTC, as determined by peak sea breeze time for both the spring and summer sea breeze cases. We limited our calculations to the 2-D trajectories as vertical velocities were *O*(100) times smaller than horizontal velocities during the sea breeze cases analyzed.

Numerous metrics exist to map LCSs from the trajectories, including finite time Lyapunov exponent, finite size Lyapunov exponent, and relative dispersion (RD; Haller, 2015). Here we have chosen to use RD, defined as the mean separation distance between particles after a certain finite amount of time. Barriers, or lines with high values of RD, separate regions in which particles remain near each other. Particles that begin on the barrier end up on either side of the barrier, thus producing the high RD values right on the barrier.

RD is calculated at each spatial point by taking the mean distance between the particle released at a point and its four nearest neighbors after each 1-hr simulation. For example, all particles are initially 10 km apart; after 1 hr a chosen particle is 9, 11, 13, and 15 km away from its original four nearest neighbors (Figure 5), resulting in

$$\mathrm{RD} = (9\mathrm{km} + 11\mathrm{km} + 13\mathrm{km} + 15\mathrm{km})/4 = 12\mathrm{km}.$$

RD minus the initial 10-km separation distance of the particles is used in Figures 6, 7, 9, and 10. RD-10 km represents the mean rate of separation of particles relative to the initial separation distance. This provides a speed (km/hr) of divergence and convergence.

2.5. Description of Test Cases

Two sea breeze cases were used in this study. Both cases were *pure* sea breezes; that is, their largest synoptic wind component throughout the sea breeze time (1700–0000 UTC) was perpendicular to the coastline and directed offshore. A WRF vertical level of 925 Mb was chosen as the height to determine

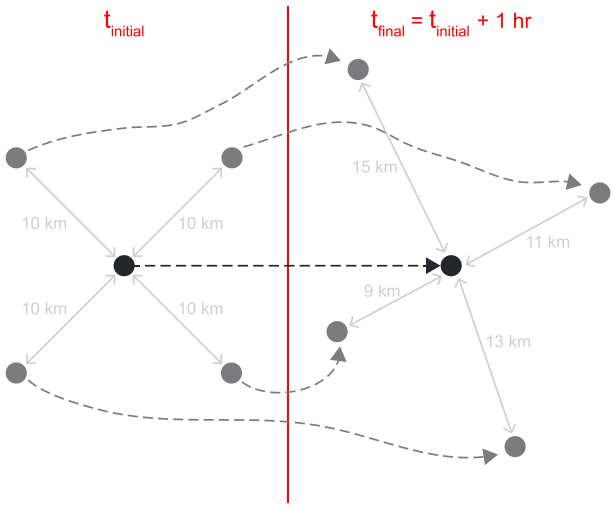

Figure 5. Graphic depicting relative dispersion (RD) example as described in text. Dots on left ($t_{initial}$) show tracers with black dot in center starting 10 km away from its four nearest neighbors (dark gray). Black and dark gray dashed arrows show tracer trajectories over 1 hr, and dots on right (t_{final}) show ending position of tracers.

the synoptic wind, consistent with Steele et al. (2014). As stated above, pure sea breezes are likely to be secondary to corkscrew in NJ based on a short-term synoptic wind climatology study for the MAB. However, the selection of two *pure* sea breeze cases for this study is important because the cross sections will be parallel to the dominant synoptic flow component, thus making the synoptic flow sensitivities clear, effective, and impactful.

The first sea breeze case occurred in the spring on 27 April 2013 with no coastal upwelling (Figure 1); this sea breeze falls in the period before the upwelling season begins (Figure 4). This case will be used to verify our application of the new Lagrangian technique, and will be used to test the limits of the offshore extent when the onshore front propagates all the way across the state of NJ. This *pure* sea breeze occurred with light synoptic wind conditions from the northwest. The spring thermal contrast between the cold waters (8–10 °C) across the entire MAB continental shelf (water depths less than 200 m) and the warming land surfaces (Figure 1a) produced an air temperature difference of nearly 8 °C when comparing NDBC 44009 air temperature to KACY 2mT (Figure 1b). A simulation using the WRF model showed a skin temperature difference at 1700 UTC of at least double this air temperature difference (Figure 1a).

The second sea breeze case occurred in the summer on 13 August 2012 during active coastal upwelling (Figure 3); this sea breeze falls in the middle of the upwelling season (Figure 4). This *pure* sea breeze case will be used to perform both the synoptic flow and upwelling sensitivities. For the synoptic flow sensitivity, weak synoptic offshore flow occurred over the Delmarva Peninsula with large inland frontal propagation, and strong synoptic offshore flow over NJ with the inland sea breeze front stalling near the coastline. For the upwelling sensitivity, a WRF simulation performed with 13 August 2012 upwelling SST conditions (Figure 3b) was compared to another WRF simulation using two days prior 11 August 2012 nonupwelling SST conditions (Figure 3a). Air temperature differences between land and water approached 4 °C during both the nonupwelling day and upwelling day (Figure 3c), while skin surface temperature differences between land and water approached 10 °C during the nonupwelling afternoon (Figure 3a) and 12 °C during the upwelling day afternoon (Figure 3b).

3. Results

3.1. Sea Breeze Case 1: 27 April 2013

During clear-air mode, KDIX weather radar base elevation scans first captured a sea breeze front stretching along and just inshore of the NJ coastline at ~1600 UTC on 27 April 2013. The front propagated inland to just east of the KDIX radar location at 1700 UTC (Figure 6a), to just west of KDIX at 2000 UTC (Figure 6c), to near Trenton, NJ, at 2300 UTC (Figure 6e), dissipating just west of Philadelphia, PA, at ~0000 UTC on 28 April 2013.

RD mapped at 100 m at the same times (1700, 2000, and 2300 UTC) show a similar inshore picture (Figures 6b, 6d, and 6f). Vectors show Eulerian WRF 100-m horizontal winds averaged across the hour beginning at the time indicated on the panel (e.g., winds averaged across 1700–1800 UTC for Figure 6b). These vectors provide a traditional display of winds fixed on the WRF grid as they evolve with the sea breeze circulation. Red and blue shading indicate RD minus the initial 10-km separation distance of the particles, providing a speed (km/hr) of divergence (red) and convergence (blue). Based on the convectional theory of the sea breeze, blue convergent areas at 100 m should align with the inland sea breeze front and red divergent areas at 100 m should align with the offshore sea breeze divergence zone. The yellow dot indicates weather radar-captured position of the inland sea breeze front along the NW to SE cross-section black line. The height of 100 m was chosen for WRF winds and RD results because (a) the maximums in onshore convergence and offshore divergence are most pronounced at this height, (b) the wind speed vectors are stronger at 100 m than at 10 m, and (c) 100 m corresponds to approximate hub height of offshore wind turbines, making this work more broadly applicable. The conclusions are insensitive to the choice of height as long as the choice is within the lower portion of the sea breeze circulation, or <~500 m.

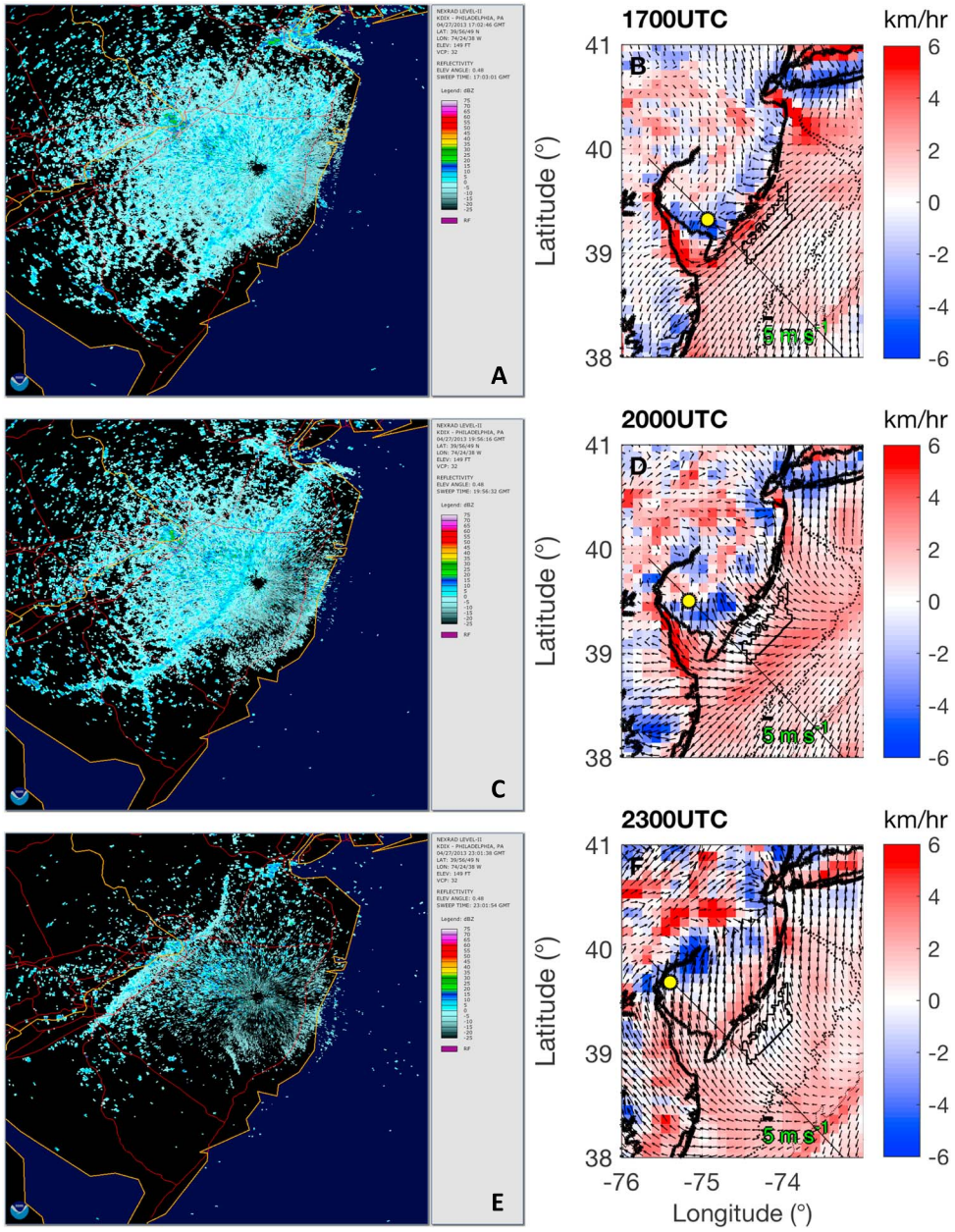

Figure 6. 27 April 2013. KDIX weather radar (located at black dot in middle of the data field) base elevation scan in (left) clear-air mode at (top) 1700, (middle) 2000, and (bottom) 2300, showing inland propagation of sea breeze front. RD-10 km (km/hr) at 100 m, or mean rate of separation relative to the initial 10-km separation distance, shaded red (divergence) and blue (convergence) at right and at the same three times. NJ WEA marked in black boxed contour, 50-m isobath in thick dotted black contour, 200-m isobath in thin dotted black contour, cross-section location used in figures below plotted NW to SE in black, yellow dot representing intersection of weather radar sea breeze front with cross section, and green 5 m/s legend scale vector for black WRF 100-m wind vectors averaged across the hour beginning at time indicated on panel.

At 1700 UTC, the blue convergence zone stretches just inshore of the NJ coast, and aligns well with the weather radar front (Figure 6b). Convergent areas are also apparent along the Delmarva and Long Island coastlines. Offshore there is a broad area of red divergence, with local maxima in divergence just offshore of NJ, in the Delaware Bay, and just offshore of Raritan Bay. Three hours later at 2000 UTC, the convergent area has progressed farther onshore with the weather radar sea breeze front, and the divergent area has progressed farther offshore, now southeast of the NJ WEA (Figure 6d). Finally, at 2300 UTC, the convergent area

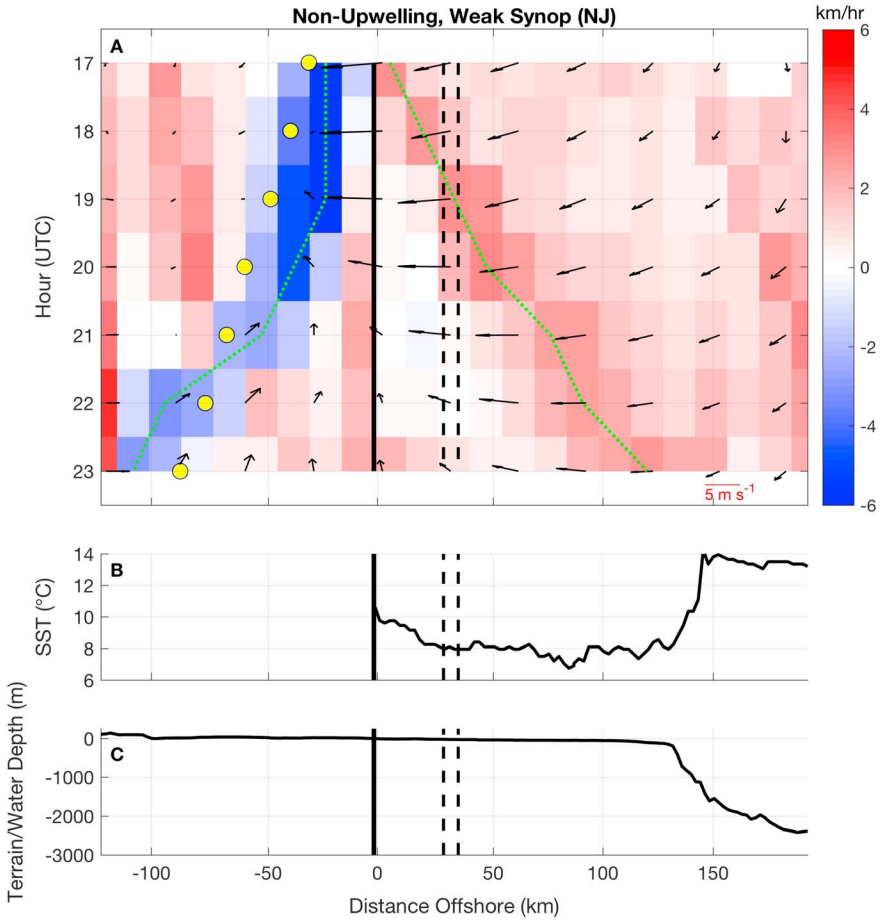

Figure 7. 27 April 2013. (a) Hövmoller diagram of RD-10 km (km/hr) averaged across 50, 100, and 150 m shaded for the nonupwelling weak synoptic condition (NJ) case, 27 April 2013, along the cross section indicated in Figures 6b, 6d, and 6f; red shading for divergence and blue shading for convergence. Black vectors represent averaged WRF wind vectors across 50, 100, and 150 m, and across hour beginning at time indicated on *y* axis. Green dotted line traces maximum convergence onshore and maximum divergence within 150 km offshore. Black solid vertical line marks the coast, and two black dashed vertical lines mark the inshore and offshore boundaries of the NJ WEA. (b) SST (°C) along the cross section. (c) Terrain height (m) onshore and water depth (m) offshore along the cross section.

has progressed all the way to the Delaware River/Philadelphia with the weather radar front, and the divergent area has propagated offshore to southeast of the 200-m isobath (black; Figure 6f). Inshore of the red divergent area there is a zone of white, indicating neither divergence nor convergence in the Lagrangian wind field. At all three times, the inland blue RD convergent areas (Figures 6b, 6d, and 6f) are much more extensive than the front observed by radar (Figures 6a, 6c, and 6e). This is likely due to the much lower temporal resolution of the RD analyses (1 hr) versus the radar image [*O* (minutes)].

A Hövmoller diagram along the cross section indicated by the black line in Figures 6b, 6d, and 6f is depicted in Figure 7a. Figure 7b shows SST (°C) under the same cross section, with SST uniformly cold across the entire shelf out to ~130 km offshore, increasing in temperature in the deep water off the shelf. The blue convergence zone begins ~25 km onshore at 1700 UTC, slowly propagating farther onshore to >100 km onshore at 2300 UTC and well aligned with the yellow weather radar dot (Figure 7a). This is highlighted by the green dotted trace of the maximum blue convergence. The red divergence zone begins just offshore of the coast and propagates farther offshore, reaching almost to the shelf break by 2300 UTC, and again highlighted by the green dotted trace of maximum divergence. This maximum divergence—what we use as the offshore extent of the sea breeze cell—crosses the NJ WEA at ~1900 UTC. The propagation of the sea breeze front onshore is slower than the propagation of the sea breeze cell offshore, especially earlier on at 1700–2000 UTC. This asymmetric propagation pattern may be attributed to a difference in turbulence/frictional effect

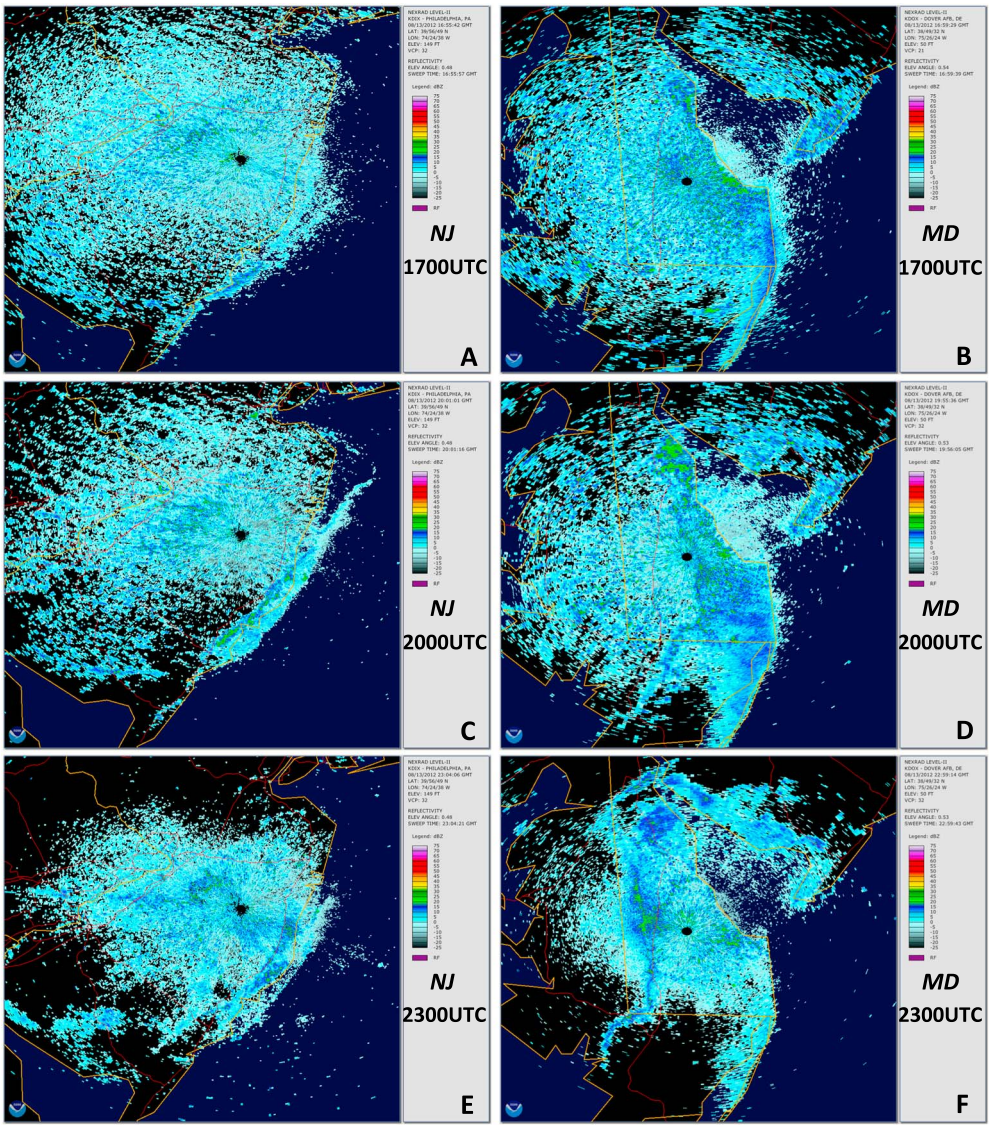

Figure 8. 13 August 2012. Same as in Figure 6 left panel but for the 13 August 2012 upwelling case, with NJ on left and MD on right.

between land and sea (Jiang et al., 2017; Sha et al., 1991). The end result is that the sea breeze cell begins at a width of about 30 km centered on the coast and slowly and relatively symmetrically expands onshore and offshore to about a width of nearly 250 km after 7 hr.

3.2. Sea Breeze Case 2: 13 August 2012

At the same three times as the weather radar imagery for the 13 August 2012 sea breeze case (Figure 8), RD results at 100 m are shown in Figure 9. The left panel in Figure 9 shows WRF and RD results for upwelling conditions, and the right panel for the nonupwelling conditions. The stalled out front over the NJ coastline is again apparent in the blue convergence shading for both upwelling and nonupwelling, with the convergence zone expanding in size onshore through time. Over the Delmarva Peninsula, the convergence zone propagates inland with the yellow weather radar dot. Offshore, though more subtle than the 27 April 2013 case, the divergence zone can be seen propagating offshore along the NJ cross section line, and much more clearly can be seen propagating offshore of the Delmarva Peninsula. Comparing upwelling to nonupwelling shows darker red divergence for the upwelling case at all three times and for both the NJ and Delmarva sea breezes, while onshore, differences in convergence intensities are less apparent. Small differences in

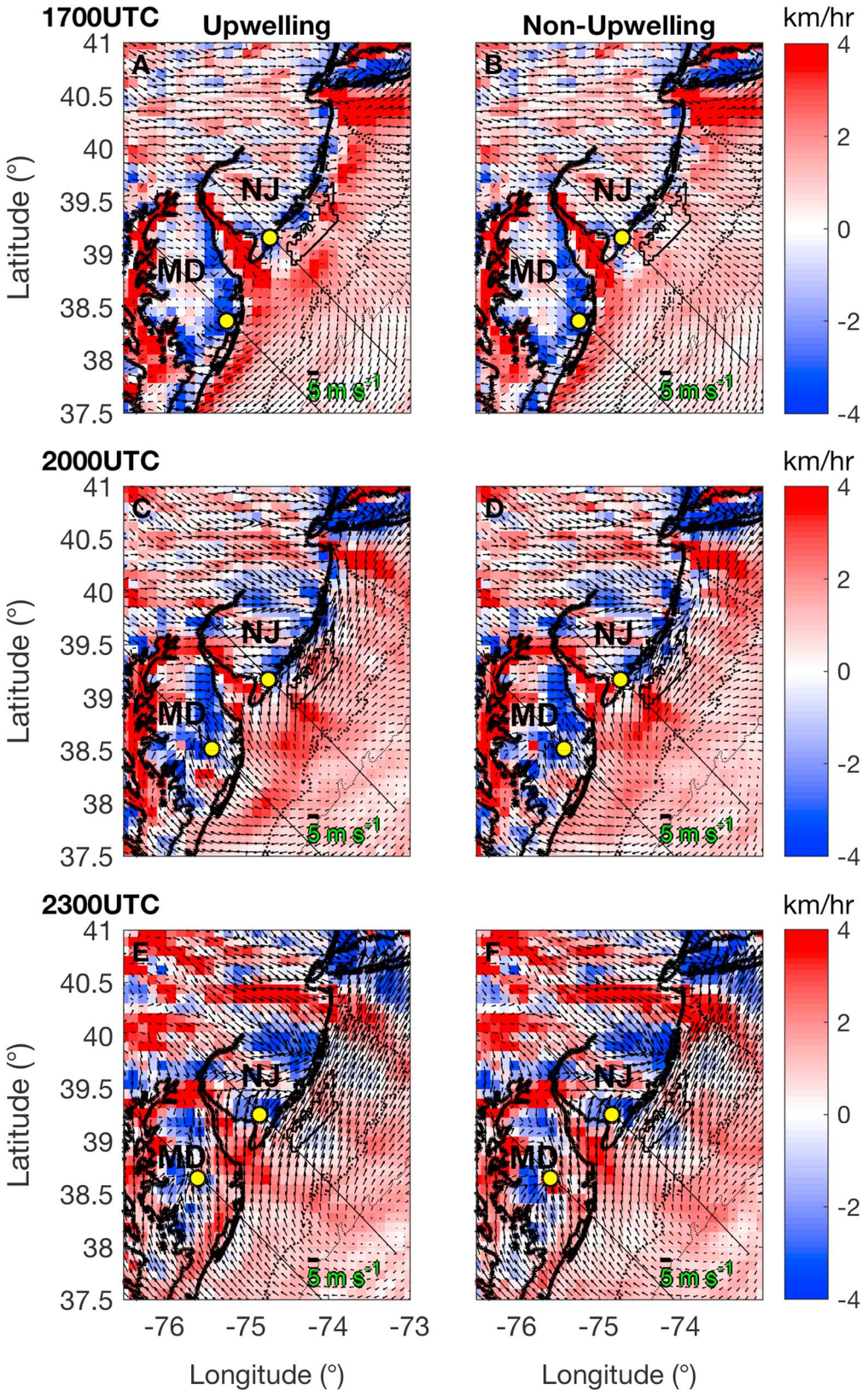

Figure 9. 13 August 2012. Same as in Figure 6 right panel but for the 13 August 2012 upwelling case, with results from the WRF simulation using upwelling SST conditions on left, and from the WRF simulation using nonupwelling SST conditions from two days prior on 11 August 2012 on right. Cross-section location for both NJ and MD are shown, with yellow dots marking the intersection of the respective weather radar inland sea breeze front with the cross section.

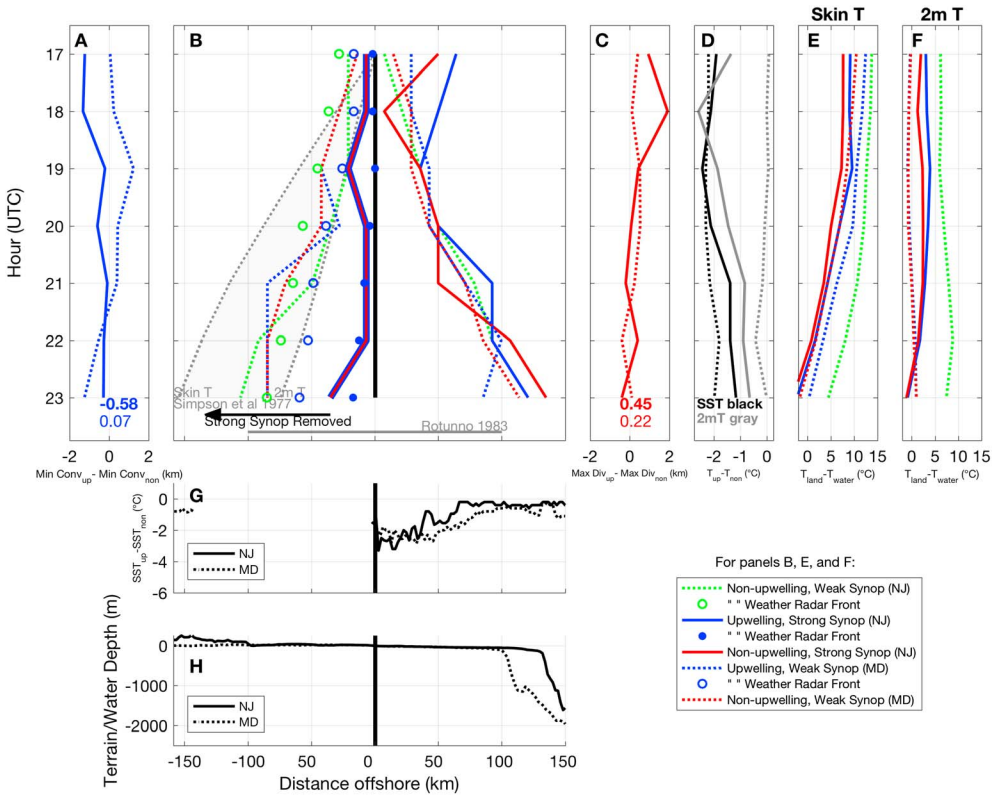

Figure 10. Composite of both sea breeze cases. (b) Hövmoller traces of maximum convergence onshore and maximum divergence offshore, preserving the same coloring from Figure 7. Weather radar frontal locations marked by open green circle for nonupwelling weak synoptic conditions (NJ), open blue circle for upwelling weak synoptic conditions (MD), and closed blue circle for upwelling strong synoptic conditions (NJ). Black vertical line represents the coast, and gray ribbon represents Simpson et al. (1977) linear theory of inland sea breeze propagation using WRF skin temperature (gray dotted left boundary) and 2mT (gray dotted right boundary). Black arrow pointing left and labeled "Strong Synop Removed" indicates the distance onshore that the solid blue and red lines would have traveled if the synoptic wind along the cross section were removed. Horizontal gray line represents sea breeze linear theory for horizontal extent from Rotunno (1983). For strong (solid) and weak (dotted) synoptic conditions, (a) time series of upwelling minimum convergence (averaged across three grid cells around minimum) minus nonupwelling minimum convergence and (c) time series of upwelling maximum divergence minus nonupwelling maximum divergence. (d) For strong (solid) and weak (dotted) synoptic conditions, time series of upwelling SST minus nonupwelling SST (black) and the same for 2mT (gray), averaged from coast to offshore extent in (b). $T_{Land} - T_{Water}$ time series using (e) skin temperature and (f) 2mT, averaged from coast to onshore extent for T_{Land}, and from coast to offshore extent for T_{Water} in (b). (g) Upwelling SST minus nonupwelling SST (°C) for NJ (solid black) and MD (dotted black) under cross sections. (h) Terrain height (m) onshore and water depth (m) offshore for NJ (solid black) and MD (dotted black).

propagating speeds and extents on both the onshore and offshore sides exist between upwelling and nonupwelling. Comparing synoptic flow strength, for strong synoptic flow at NJ, inland blue convergence remains stationary, while the offshore red divergence propagates offshore (Figures 9e and 9f); for weak synoptic flow at MD, inland blue convergence propagates inland, while the offshore red divergence propagates offshore (Figures 9e and 9f).

3.3. Composite of Sea Breeze Sensitivities

A composite of the Hövmoller traces from the 27 April 2013 spring sea breeze case (Figure 7) and the 13 August 2012 summer sea breeze case is depicted in Figure 10b. For sea breeze extent sensitivity to synoptic flow, the inshore side is sensitive with all dotted lines representing weak synoptic flow propagating at approximately the same speed, ending at ~80–110 km onshore, and both solid lines representing strong synoptic flow stalling close to the coastline (within ~40 km) and not propagating onshore against the strong offshore synoptic wind. The offshore side is not as sensitive to synoptic flow, with both dotted and solid lines

all propagating well offshore to the shelf break and beyond, ending between ~80 and 130 km offshore. However, strong synoptic flow does increase offshore extent through the lifetime of the sea breeze cell, especially for upwelling—average distance offshore across all 7 hr is increased from 57 km offshore (weak synoptic) to 72 km offshore (strong synoptic) for upwelling, and from 55 km offshore (weak synoptic) to 62 km offshore (strong synoptic) for nonupwelling.

For sea breeze extent sensitivity to upwelling, both the inshore and offshore sides are only slightly sensitive. The red and blue dotted and solid line pairs are more or less aligned with each other throughout the entire 7-hr period (Figure 10b), with slight increases in average offshore extent through the sea breeze cell's lifetime due to upwelling, especially for strong synoptic flow—from 62 km offshore (nonupwelling) to 72 km offshore (upwelling) for strong synoptic, and from 55 km offshore (nonupwelling) to 57 km offshore (upwelling) for weak synoptic. As will be shown next, upwelling does have a large impact on the intensity of the sea breeze cell.

For the strong synoptic (NJ) case for both onshore convergence (Figure 10a) and offshore divergence (Figure 10c), upwelling produces a more intense sea breeze on both sides of the circulation. For the weak synoptic (MD) case, the sensitivity of sea breeze intensity to upwelling is less as compared to the strong synoptic case (Figures 10a and 10c). These panels show the difference between upwelling and nonupwelling of the most negative convergence onshore (Figure 10a), and for the most positive divergence offshore (Figure 10c). This difference is calculated by taking the average across the three grid cells centered on the most negative convergence onshore and most positive divergence offshore, producing a sensitivity of the intensity at both sides of the sea breeze cell to upwelling. For the strong synoptic case (solid lines), upwelling produces a more intense sea breeze, especially early on, with differences in convergence of approximately −1.3 km/hr at 1800 UTC and differences in divergence approaching +2 km/hr also at 1800 UTC. This means that at 1800 UTC, upwelling increases the intensity of the convergence and divergence by a factor of almost 2.4 and 4.3, respectively. The maximum differences occur earlier in the sea breeze event while the horizontal extent of the cell is comparable to the width of the ocean upwelling region. On average, the RD difference in regions of particle attraction is −0.58, and +0.45 km/hr in regions of particle repulsion, or upwelling on average increases the intensity of the attraction by 50% and repulsion by 22% for the strong synoptic case. For the weak synoptic case, average difference is +0.07 km/hr in regions of particle attraction and +0.22 km/hr in regions of particle repulsion, meaning that upwelling has less of an influence on sea breeze intensity during weak synoptic flow.

To investigate possible reasons why the sea breeze is more intense on both the onshore and offshore sides, especially earlier on in the circulation, we turn to Figure 10d. Here the difference along the cross section in SST (black) and 2mT (gray) between upwelling and nonupwelling (Figure 10g shows SST) is used. This SST upwelling-nonupwelling difference is averaged from the coast to the blue solid (dotted) line representing the maximum divergence location and offshore extent of the strong (weak) synoptic upwelling sea breeze. This average $SST_{upwelling}$-$SST_{nonupwelling}$ difference for the strong synoptic case (solid black) peaks at nearly −3 °C at 1900 UTC, and is greater than −1 °C throughout the entire sea breeze lifetime (Figure 10d). In other words, a greater percentage of the sea breeze cell is "feeling" the upwelling underneath it earlier on when the sea breeze cell is small, until the sea breeze cell expands offshore past the upwelling and a larger proportion of the cell "feels" the effects of the warmer waters offshore of the upwelling. Similar results are attained using the 2mT upwelling-nonupwelling difference (solid gray in Figure 10d) for the strong synoptic conditions. Interestingly, for the weak synoptic conditions, 2mT upwelling-nonupwelling differences (dotted gray) are much smaller than SST (dotted black) upwelling-nonupwelling differences, indicating that 2mT differences have a more direct correlation with sea breeze intensity differences during weak synoptic conditions.

The dynamic theory of the sea breeze (Simpson et al., 1977) is shown by the gray ribbon bounded by the skin T and 2mT for land-sea temperature differences in the calculation of inland sea breeze frontal propagation speed (Figure 10b). From Simpson et al. (1977), the rate of advance of the inland sea breeze front can be expressed as

$$u = \{[T_{Land} - T_{Water}] g\, h/2\, T\}^{1/2} \quad (1)$$

where T_{Land} is the land temperature (K), T_{Water} is the sea temperature (K), g is the gravity, h is the vertical scale of the heating (350 m estimated from model), and T is a reference temperature (300 K). This behavior can be expected as long as the synoptic wind component across the coast is very small (Simpson et al., 1977). T_{Land}

and T_{Water} are based on average temperatures under the three weak synoptic wind condition cases (two nonupwelling and one upwelling; dotted lines in Figure 10b), or the sea breeze cells that are less affected by the synoptic flow. T_{Land} is calculated by taking the average skin/2mT from the coast to each of the three inland dotted lines, and averaging those three values. T_{Water} is calculated the same way but from the coast to each of the three offshore dotted lines. Assuming that the inland sea breeze front begins at the coastline, the gray dotted lines are plotted based on the speed u calculated using equation (1). Because land-sea skin temperature differences are greater than land-sea 2mT differences, the skin temperature gray dotted line has a faster inland propagation speed and ends ~150 km onshore, with the 2mT gray dotted line ending ~75 km onshore. The three colored dotted lines inland fall within the gray ribbon bounded by the two gray dotted lines, indicating that our weak synoptic results are consistent with dynamic linear theory of the sea breeze according to Simpson et al. (1977).

In order to complete the comparison with Simpson et al. (1977), synoptic winds were "removed" from the two strong synoptic condition sea breeze cases (solid red and blue inland lines). To do this, for the 13 August 2012 strong synoptic (NJ) upwelling sea breeze case, the 925-Mb horizontal wind speed component parallel to the NJ cross section was taken at the closest WRF grid point to Philadelphia, PA (KPHL), at each hour from 1700 to 2300 UTC. Then, the average of those seven values was taken, resulting in 4.56 m/s. In comparison, the 13 August 2012 weak synoptic (MD) upwelling sea breeze case taken at Ocean City, MD (KOXB), gives a value of 0.61 m/s, and the 27 April 2013 weak synoptic (NJ) nonupwelling sea breeze case taken at KPHL gives a value of 1.9 m/s. To get the inland propagation of the sea breeze that would have resulted if the strong synoptic winds were removed, the mean of 4.56 m/s was multiplied by 7 hr, with the resulting distance added to the final sea breeze inland propagation distance. This is indicated by the leftward black arrow labeled "Strong Synop Removed" in Figure 10b. Instead of stalling near the coast due to the opposing strong synoptic winds, the sea breeze inland front would have propagated ~130 km inland, within the gray (Simpson et al., 1977) ribbon.

A second comparison to dynamic linear theory of the sea breeze is plotted as the horizontal gray line at the bottom of Figure 10b labeled "Rotunno (1983)." This line indicates the horizontal extent of the sea breeze according to linear theory of motion:

$$\text{For } f > \omega \left(\text{latitudes} > 30^{\circ}\right): \quad Nh\left(f^2-\omega^2\right)^{-1/2} \tag{2}$$

where $f = 2\Omega\sin\phi$ is the Coriolis frequency, $\omega = 2\,\pi$/day is the frequency of diurnal heating of land, $N = [(g/\theta_0)(\partial\theta/\partial z)]^{1/2}$ is the Brunt-Väisälä frequency (stratification) with $\partial\theta/\partial z$ estimated at 10 K/1,000 m from temperature profile plots, and h is the vertical scale of the heating (350 m as above; Rotunno, 1983). For our sea breeze cases at latitude 40°N, we get ~100 km. This means that according to Rotunno (1983) linear theory of the sea breeze, the onshore and offshore extents of our sea breeze cases should both reach ~100 km from the coast. All weak synoptic Hövmoller traces match within this ±100-km distance from the coast, again consistent with linear dynamic theory of the sea breeze.

Figure 10e ("skin T") and Figure 10f ("2mT") show the temperature difference $T_{Land} - T_{Water}$ that the sea breezes "feel," or the thermal gradient driving each sea breeze. Again, this is calculated similar to the above, where T_{Land} is the average skin/2mT from the coast to the inland boundary and T_{Water} is the average skin/2mT from the coast to the offshore boundary. First, skin temperature differences are larger than 2mT differences for the first 4 hr. Second, the solid blue upwelling lines are always greater than the solid red nonupwelling lines, indicating a stronger thermal gradient with upwelling than without, under strong synoptic forcing. Third, for skin T, the dotted blue upwelling line is always greater than the dotted red nonupwelling line, again indicating stronger thermal gradient forcing with upwelling than without, under weak synoptic forcing.

It is also stated in Rotunno (1983) that the sea breeze has "an elliptically shaped pattern of flow in the vertical plane, centered on the coast, having an aspect ratio (vertical/horizontal scale)" given by

$$\text{For } f > \omega \left(\text{latitudes} > 30^{\circ}\right): \quad \left(f^2-\omega^2\right)^{1/2} N^{-1} \tag{3}$$

where, as before, $f = 2\Omega\sin\phi$ is the Coriolis frequency, $\omega = 2\,\pi$/day is the frequency of diurnal heating of land, and $N = [(g/\theta_0)(\partial\theta/\partial z)]^{1/2}$ is the Brunt-Väisälä frequency (stratification). For our sea breeze case at 40°N, we get ~0.0035 for the vertical/horizontal aspect ratio. For comparison, Rotunno (1983) stated an aspect ratio of

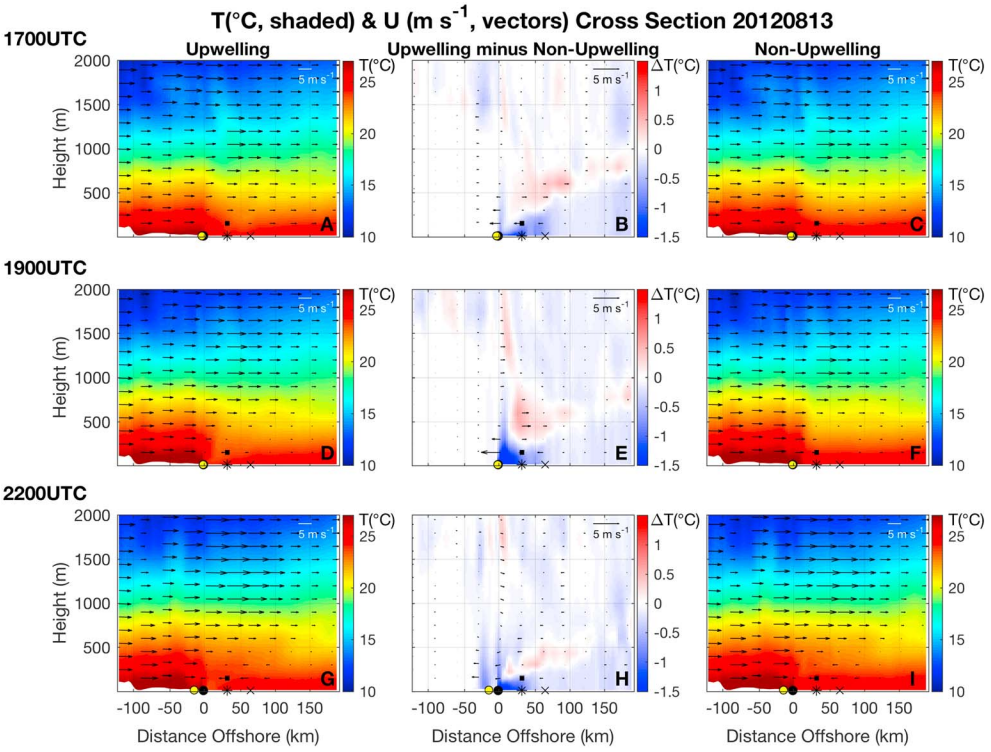

Figure 11. 13 August 2012. NJ vertical cross section (strong synoptic sea breeze) along location marked in Figures 6 and 7, with (left) upwelling, (right) nonupwelling, and (middle) upwelling minus nonupwelling, and with temperature (°C) shaded and wind vectors (m/s; both along-cross section *u* and *w* components averaged across hour beginning at time indicated at top left) in black vectors. Black dot is coast, black asterisk is at NJ WEA, black "cross" is twice the distance from coast to NJ WEA offshore, small black solid line above the asterisk at 150 m is over NJ WEA at approximate blade tip height, and yellow dot is weather radar sea breeze location. Note that wind vectors are exaggerated in middle difference plots.

0.00685 for their idealized sea breeze case at 45°N with *N* assumed to be 10^{-2} s. Our sea breeze is more vertically compact, due to differences in both latitude and *N*.

3.4. Cross Sections and Profiles

To further investigate the impact of upwelling on sea breeze intensity, vertical cross sections for the strong synoptic flow case at three different hours (1700, 1900, and 2200 UTC) were taken of temperature and the wind velocity component along the same NJ cross section used above. These cross sections for upwelling (left), nonupwelling (right), and upwelling minus nonupwelling (middle) are shown in Figure 11. Upwelling produces colder air directly above the surface, with warmer air above that at ~400–700 m, at all 3 hr plotted (Figures 11b, 11e, and 11h). The colder and warmer air regions increase in height downstream of the synoptic wind flow. Difference vectors directly above the coast show sea breeze enhancement due to upwelling up to ~750 m, and return flow enhancement >750 m in height. Also, more sinking air due to upwelling can be seen directly above the coast, especially by 2200 UTC.

Vertical profiles were taken at three locations along the cross sections: at the coast (black dot in Figure 11), at the edge of the upwelling in the NJ WEA (black asterisk), and at the offshore location (black "cross"). These vertical profiles at 1700, 1900, and 2200 UTC are shown on semilog plots in Figure 12.

These three times were chosen for their importance in the upwelling and nonupwelling sea breeze cell positioning: at 1700 UTC, the upwelling sea breeze cell onshore extent is aligned with the coast; at 1900 UTC, the nonupwelling sea breeze cell offshore extent is aligned with the offshore location; and at 2200 UTC, the nonupwelling sea breeze cell onshore extent is aligned with the coast.

At 1700 UTC, the upwelling sea breeze cell (blue) starts just over the edge of the upwelling, but has not quite expanded to the coast or offshore yet. This is indicated in the blue wind profile by near-surface negative *u*

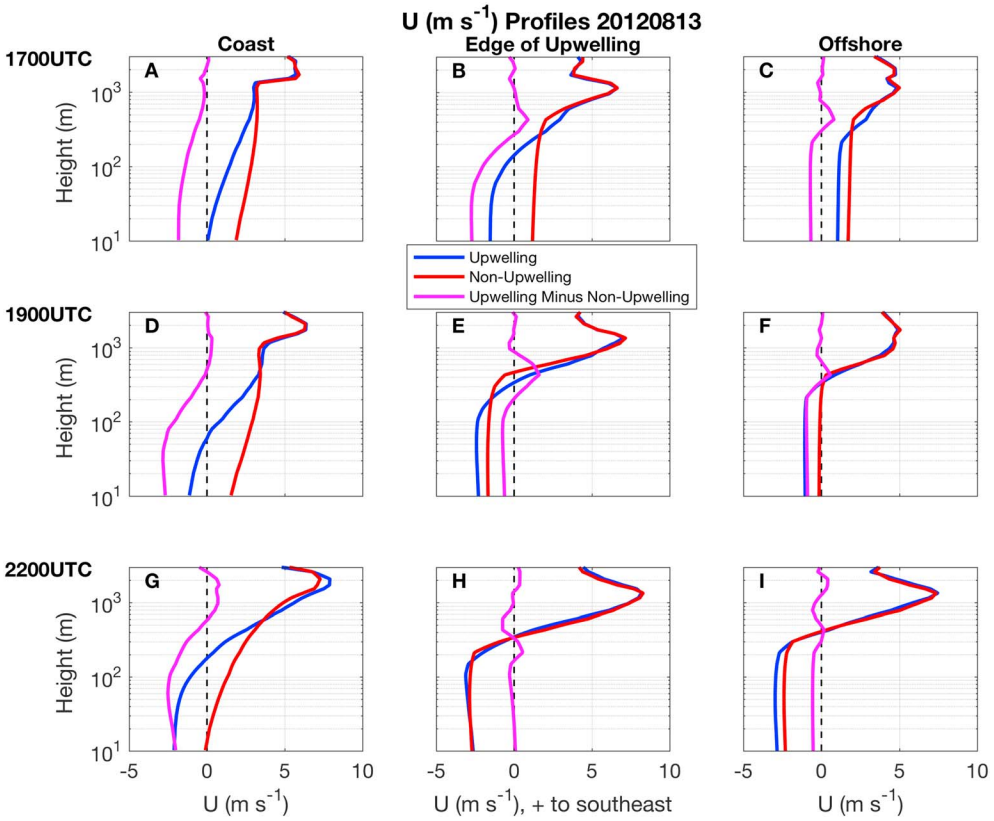

Figure 12. 13 August 2012. Vertical profiles of horizontal velocities (m/s; positive to the southeast) along cross section on semilog axes at the same times as Figure 11 and (left) at the coast, (middle) edge of upwelling/NJ WEA, and (right) offshore. Upwelling (blue), nonupwelling (red), and upwelling minus nonupwelling (magenta). Vertical dashed line marks 0 horizontal velocity.

velocities, or winds to the northwest. The nonupwelling sea breeze cell (red) onset has not occurred yet at all three locations (all positive *u* velocities). At 1900 UTC, the upwelling sea breeze cell has now expanded over all three locations, with the nonupwelling sea breeze cell at the edge of upwelling location but not yet at the other two locations. Finally, at 2200 UTC, the upwelling sea breeze cell strengthens at all three locations, and the nonupwelling sea breeze cell is at the edge of the upwelling and offshore, but not at the coast. These sea breeze cell onset, expansion, intensification, and overall evolution results can also be seen in Figure 10.

At 1700 and 1900 UTC, the upwelling sea breeze profile is shallower and sharper than the nonupwelling sea breeze profile. Then, at 2200 UTC, the sea breeze shapes eventually become similar, especially at the edge of upwelling (Figure 12h) and offshore (Figure 12i) locations.

The conclusions from the sea breeze vertical profile results are thus as follows: (a) upwelling sea breeze onset is earlier, and resulting expansion and intensification is larger and stronger; (b) upwelling sea breeze is shallower, sharper, and narrower, consistent with Clancy et al. (1979) and Bowers (2004); (c) upwelling and nonupwelling sea breeze "shape" become similar by the end of the sea breeze; and (d) the difference between the upwelling and nonupwelling sea breeze profiles (magenta profiles in Figure 12) is an enhanced sea breeze near surface and an enhanced return flow aloft; in other words, upwelling enhances the sea breeze near the surface and strengthens the return flow aloft.

4. Discussion and Summary

In this paper, the utility of Lagrangian methods to highlight, clarify, and objectively define the offshore extent of the sea breeze has been shown. We validated the LCS metric RD onshore with the weather radar frontal location, and offshore against linear sea breeze theory and expected cell expansion and propagation. The

new validated metric allowed us to clearly and accurately characterize the sea breeze circulation cell both onshore and offshore. Then, sensitivities of sea breeze extent and intensity to synoptic wind strength (atmospheric sensitivity) and upwelling (ocean sensitivity) were performed. Sea breeze extent sensitivities will be summarized, discussed, and compared with past studies in the next two paragraphs, and sea breeze intensity sensitivities will be reviewed thereafter.

The inland extent of a *pure* sea breeze was found to be very sensitive to synoptic flow strength, and the offshore sea breeze extent was found to be less sensitive, consistent with Finkele (1998). One possible reason for this is that the inland sea breeze side is encountering the strong offshore synoptic flow, creating a wake that prevents any large influence on the downstream offshore side. The offshore extent, when affected, was more sensitive to strong synoptic flow during upwelling. The synoptic flow sensitivity results here also agree with Arritt (1993), who found that synoptic wind conditions produced large shifts in the position of the sea breeze circulation, with the circulation existing entirely offshore if the opposing flow is strong. In the strong synoptic case here, the sea breeze cell existed almost entirely offshore, with the inland extent just onshore of the coast and the offshore extent approaching 150 km offshore by the end of the simulation for both upwelling and nonupwelling (Figure 10). Finally, in this study, the sea breeze's offshore extent at 100-m height was ~3 times greater than its onshore extent during strong synoptic flow conditions, and the onshore/offshore extents were about equal during weak synoptic flow conditions. These results agree with Bowers (2004), who found that the offshore extent was roughly 2 to 3 times that of the inland penetration during a stronger synoptic wind condition.

Upwelling slightly increased the offshore extent of the sea breeze, especially during strong synoptic conditions, possibly due to the strong flow "pushing" the circulation farther offshore and thus allowing upwelling to intensify the sea breeze and slightly widen it. Overall, though, upwelling did not have any significant impact on either onshore or offshore sea breeze extent, in contrast to Clancy et al. (1979) who found in their two-dimensional idealized model study that upwelling sea breeze "penetrates more than twice as far inland than it would without the upwelling." Bowers (2004) found that for their strong offshore synoptic flow case study, upwelling forced the inland sea breeze front to penetrate 6 to 18 km farther onshore than without upwelling, and for their weak offshore synoptic flow case study, upwelling produced no significant difference in inland sea breeze penetration. The results here are thus in general agreement with Bowers (2004).

While upwelling did not significantly influence the onshore or offshore sea breeze extent, it did have an impact on sea breeze intensity, with stronger convergence onshore and stronger divergence offshore during upwelling and strong synoptic conditions. For strong synoptic conditions, the sea breeze intensity starts much stronger with upwelling, with the upwelling minus nonupwelling sea breeze intensity difference gradually decreasing as the sea breeze cell expands outward and offshore of the upwelling. For weak synoptic conditions, upwelling overall has less of an influence on sea breeze intensity, possibly due to weaker flow allowing the sea breeze cell to remain farther inland and limiting upwelling's overall influence on the cell. Further, upwelling during strong synoptic conditions caused an earlier sea breeze onset, and a shallower, sharper, and narrower sea breeze profile, consistent with idealized modeling (Clancy et al., 1979), observations and modeling for Brazil (Franchito et al., 1998), and prior studies specific to NJ (Bowers, 2004).

Using high-frequency radar surface ocean current data, Hunter et al. (2007) found that diurnal wind-forced motions in the NJ coastal ocean associated with the sea/land breeze system can extend as far as 100 km offshore. These results are consistent with findings here, which show that the maximum divergence in the RD field propagates to approximately 100–150 km offshore, regardless of synoptic wind conditions. Further, the maximum offshore divergence at 100-m hub height crosses the NJ WEA 30–40 km offshore at ~1900 UTC, regardless of synoptic wind or upwelling conditions. The intensity of the offshore sea breeze side, however, varies at the time of NJ WEA crossing, with upwelling producing stronger offshore divergence as compared to nonupwelling conditions.

As shown here, the MAB Cold Pool has a strong influence on the sea breeze circulation across the seasons, and likely dictates the bimodal seasonal peaks in sea breeze occurrence (Figure 4). In the winter, the cold water across the entire MAB shelf forms, setting the stage; in the spring, the cold water remains across the shelf while the land warms up, leading to frequent sea breezes (Figure 4); and in the summer and early fall, the cold water is upwelled through to the surface, directly impacting the coastal land-sea thermal gradient and thus size and intensity of the frequent sea breezes (Figure 4).

Future studies should explore more in depth the specific air-sea interaction processes between upwelling and sea breeze, and across the seasons and sea breeze types. These studies should also determine the effect of sinking air and offshore surface divergence on the surface current and wavefield in the ocean. To accomplish this, RD could be calculated on high-frequency radar surface current fields to see if any coherent boundaries or areas of repulsion in the surface ocean align with the RD maximum particle repulsion in surface winds for the offshore sea breeze extent. Also, in contrast to the 2-D Lagrangian analyses performed here, future studies can include 3-D Lagrangian analyses on both the atmosphere (WRF) and ocean (Regional Ocean Modeling System) to better understand the air-sea interaction in the sea breeze-coastal upwelling system. Other Lagrangian methods, such as hyperbolic, parabolic, and elliptic LCSs (Haller, 2015), which return material features, could be used to further the study of the sea breeze. Finally, sea breeze duration and its sensitivities to synoptic flow and upwelling should be investigated, so that the offshore wind industry is aware of when and where the sea breeze will occur, and for how long it may affect wind energy production. It will continue to be critical to further study the complex and competing feedback within the sea breeze-coastal upwelling system at the land-sea coastal interface, where dynamic thermal interactions are paramount for accurately assessing and predicting resources for coastal/offshore energy systems.

Acknowledgments

NDBC buoy, surface, NEXRAD, and U.S. Coastal Relief Model data used in this study can be accessed at ndbc.noaa.gov, ncdc.noaa.gov, https://www.ncdc.noaa.gov/nexradinv/, and ngdc.noaa.gov/mgg/coastal/crm.html, respectively. AVHRR declouded data, SST composites, WRF results, and RD results can be accessed at marine.rutgers.edu/cool/weather/seroka/JGR_atmo_2018/. Support was provided by New Jersey Board of Public Utilities (2010RU-COOL, BP-070), NOAA-led Integrated Ocean Observing System (IOOS) through the Mid-Atlantic Regional Association Coastal Ocean Observing System (MARACOOS; NA11NOS0120038), and Rutgers University. Louis Bowers assisted with WRF simulations; John Wilkin provided suggestions on comparisons with past studies; and Mike Crowley, John Kerfoot, and Laura Palamara Nazzaro supported the satellite SST analyses.

References

Arritt, R. W. (1989). Numerical modelling of the offshore extent of sea breezes. *Quarterly Journal of the Royal Meteorological Society*, *115*(487), 547–570. https://doi.org/10.1002/qj.49711548707

Arritt, R. W. (1993). Effects of the large-scale flow on characteristic features of the sea breeze. *Journal of Applied Meteorology*, *32*(1), 116–125. https://doi.org/10.1175/1520-0450(1993)032<0116:EOTLSF>2.0.CO;2

Atlas, D. (1960). Radar detection of the sea breeze. *Journal of Meteorology*, *17*(3), 244–258. https://doi.org/10.1175/1520-0469(1960)017<0244:RDOTSB>2.0.CO;2

Bigelow, H. B. (1933). Studies of the waters on the continental shelf, Cape Cod to Chesapeake Bay: I. The cycle of temperature. *Papers in Physical Oceanography and Meteorology*, *2*(4), 1933–1912. https://doi.org/10.1575/1912/1144, (December)

Bowers, L. (2004). The effect of sea surface temperature on sea breeze dynamics along the Coast of New Jersey, Rutgers University.

Castelao, R., Glenn, S., Schofield, O., Chant, R., Wilkin, J., & Kohut, J. (2008). Seasonal evolution of hydrographic fields in the central Middle Atlantic Bight from glider observations. *Geophysical Research Letters*, *35*, L03617. https://doi.org/10.1029/2007GL032335

Clancy, R. M., Thompson, J. D., Hurlburt, H. E., & Lee, J. D. (1979). A model of mesoscale air-sea interaction in a sea breeze-coastal upwelling regime. *Monthly Weather Review*, *107*(11), 1476–1505. https://doi.org/10.1175/1520-0493(1979)107<1476:AMOMAS>2.0.CO;2

De Freitas, C. R. (1990). Recreation climate assessment. *International Journal of Climatology*, *10*(1), 89–103.

Dunk, R., & Glenn, S. M. (2013). An Advanced Atmospheric/Ocean Assessment Program Designed to Reduce the Risks Associated with Offshore Wind Energy Development Defined by the NJ Energy Master Plan and the NJ Offshore Wind Energy Economic Development Act: Phase I, New Brunswick, NJ.

Dvorak, M. J., Corcoran, B. A., Ten Hoeve, J. E., Mcintyre, N. G., & Jacobson, M. Z. (2013). US East Coast offshore wind energy resources and their relationship to peak-time electricity demand. *Wind Energy*, *16*(7), 977–997. https://doi.org/10.1002/we

Finkele, K. (1998). Inland and offshore propagation speeds of a sea breeze from simulations and measurements. *Boundary-Layer Meteorology*, *87*(2), 307–329. https://doi.org/10.1023/A:1001083913327

Franchito, S. H., Rao, V. B., Stech, J. L., & Lorenzzetti, J. A. (1998). The effect of coastal upwelling on the sea-breeze circulation at Cabo Frio, Brazil: A numerical experiment. *Annales de Geophysique*, *16*(7), 866. https://doi.org/10.1007/s005850050656

Gildor, H., Fredj, E., Steinbuck, J., & Monismith, S. (2009). Evidence for submesoscale barriers to horizontal mixing in the ocean from current measurements and aerial photographs. *Journal of Physical Oceanography*, *39*(8), 1975–1983. https://doi.org/10.1175/2009JPO4116.1

Glenn, S., et al. (2004). Biogeochemical impact of summertime coastal upwelling on the New Jersey shelf. *Journal of Geophysical Research*, *109*, C12S02. https://doi.org/10.1029/2003JC002265

Glenn, S. M., Crowley, M. F., Haidvogel, D. B., & Song, Y. T. (1996). Underwater observatory captures coastal upwelling events off New Jersey. *Eos (Washington. DC)*, *77*(25), 233–240.

Glenn, S. M., Miles, T. N., Seroka, G. N., Xu, Y., Forney, R. K., Yu, F., et al. (2016). Stratified coastal ocean interactions with tropical cyclones. *Nature Communications*, *7*. (08 March 2016), doi:https://doi.org/10.1038/ncomms10887

Gong, D., Kohut, J. T., & Glenn, S. M. (2010). Seasonal climatology of wind-driven circulation on the New Jersey shelf. *Journal of Geophysical Research*, *115*, C04006. https://doi.org/10.1029/2009JC005520

Haller, G. (2015). Lagrangian coherent structures. *Annual Review of Fluid Mechanics*, *47*(1), 137–162. https://doi.org/10.1146/annurev-fluid-010313-141322

Haller, G., & Yuan, G. (2000). Lagrangian coherent structures and mixing in two-dimensional turbulence. *Physica D: Nonlinear Phenomena*, *147*(3-4), 352–370. https://doi.org/10.1016/S0167-2789(00)00142-1

Hong, S.-Y., Dudhia, J., & Chen, S.-H. (2004). A revised approach to ice microphysical processes for the bulk parameterization of clouds and precipitation. *Monthly Weather Review*, *132*(1), 103–120. https://doi.org/10.1175/1520-0493(2004)132<0103:ARATIM>2.0.CO;2

Houghton, R. W., Schlitz, R., Beardsley, R. C., Butman, B., & Chamberlin, J. L. (1982). The Middle Atlantic Bight cold pool: Evolution of the temperature structure during summer 1979. *Journal of Physical Oceanography*, *12*(10), 1019–1029. https://doi.org/10.1175/1520-0485

Hunter, E., Chant, R., Bowers, L., Glenn, S., & Kohut, J. (2007). Spatial and temporal variability of diurnal wind forcing in the coastal ocean. *Geophysical Research Letters*, *34*, L03607. https://doi.org/10.1029/2006GL028945

Jiang, P., Wen, Z., Sha, W., & Chen, G. (2017). Interaction between turbulent flow and sea breeze front over urban-like coast in large-eddy simulation. *Journal of Geophysical Research – Atmospheres*, *122*(10), 5298–5315. https://doi.org/10.1002/2016JD026247

Lalas, D. P., Asimakopoulos, D. N., & Deligiorgi, D. G. (1983). Sea-breeze circulation and photochemical pollution in Athens. *Greece*, *17*(9), 1621–1632.

Miller, S. T. K., Keim, B. D., Talbot, R. W., & Mao, H. (2003). Sea breeze: Structure, forecasting, and impacts. *Reviews of Geophysics*, *41*(3), 1011. https://doi.org/10.1029/2003RG000124

Munoz-Esparza, D., & Canadillas, B. (2012). Forecasting the diabatic offshore wind profile at FINO1 with the WRF mesoscale model. *DEWI Magazine*, *40*, 73–79.

Nakanishi, M., & Niino, H. (2004). An improved Mellor-Yamada Level-3 model with condensation physics: Its design and verification. *Boundary-Layer Meteorology*, *112*(1), 1–31. https://doi.org/10.1023/B:BOUN.0000020164.04146.98

Nakanishi, M., & Niino, H. (2006). An improved Mellor–Yamada level-3 model: Its numerical stability and application to a regional prediction of advection fog. *Boundary-Layer Meteorology*, *119*(2), 397–407. https://doi.org/10.1007/s10546-005-9030-8

NOAA National Centers for Environmental Information (2017). NOAA National Weather Service (NWS) Radar Operations Center (1991): NOAA Next Generation Radar (NEXRAD) Level 2 Base Data, doi:https://doi.org/10.7289/V5W9574V.

NOAA National Geophysical Data Center (1999). U.S. coastal relief model—Northeast Atlantic, doi:https://doi.org/10.7289/V5MS3QNZ. Available from: http://www.ngdc.noaa.gov/mgg/coastal/crm.html

Papanastasiou, D. K., Melas, D., Bartzanas, T., & Kittas, C. (2010). Temperature, comfort and pollution levels during heat waves and the role of sea breeze. *International Journal of Biometeorology*, *54*(3), 307–317. https://doi.org/10.1007/s00484-009-0281-9

Pielke, R. A. (1991). Regional and mesoscale meteorological modeling as applied to air quality studies. In *Air Pollution Modeling and Its Application VIII*, (pp. 259–289). New York: Plenum Press.

Ratcliff, M. A., Petersen, R. L., Dunk, R., & DeToro, J. (1996). *Comparison of Wind Tunnel and ISDM Model Simulations of Sea Breeze Fumigation*. Atlanta, GA: Air & Waste Management Association.

Rothermel, R. C. (1983). How to predict the spread and intensity of forest and range fires.

Rotunno, R. (1983). On the linear theory of the land and sea breeze. *Journal of the Atmospheric Sciences*, *40*(8), 1999–2009. https://doi.org/10.1175/1520-0469(1983)040<1999:OTLTOT>2.0.CO;2

Sha, W., Kawamura, T., & Ueda, H. (1991). A numerical study on sea/land breezes as a gravity current: Kelvin–Helmholtz billows and inland penetration of the sea-breeze front. *Journal of the Atmospheric Sciences*, *48*(14), 1649–1665. https://doi.org/10.1175/1520-0469(1991)048<1649:ANSOSB>2.0.CO;2

Simpson, J. E., Mansfield, D. A., & Milford, J. R. (1977). Inland penetration of sea-breeze fronts. *Quarterly Journal of the Royal Meteorological Society*, *103*(435), 47–76. https://doi.org/10.1002/qj.49710343504

Steele, C. J., Dorling, S. R., Von Glasow, R., & Bacon, J. (2013). Idealized WRF model sensitivity simulations of sea breeze types and their effects on offshore windfields. *Atmospheric Chemistry and Physics*, *13*(1), 443–461. https://doi.org/10.5194/acp-13-443-2013

Steele, C. J., Dorling, S. R., von Glasow, R., & Bacon, J. (2014). Modelling sea-breeze climatologies and interactions on coasts in the southern North Sea: Implications for offshore wind energy. *Quarterly Journal of the Royal Meteorological Society*. n/a-n/a, doi:https://doi.org/10.1002/qj.2484

Tang, W., Chan, P. W., & Haller, G. (2011a). Lagrangian coherent structure analysis of terminal winds detected by lidar. Part I: Turbulence structures. *Journal of Applied Meteorology and Climatology*, *50*(2), 325–338. https://doi.org/10.1175/2010JAMC2508.1

Tang, W., Chan, P. W., & Haller, G. (2011b). Lagrangian coherent structure analysis of terminal winds detected by lidar. Part II: Structure evolution and comparison with flight data. *Journal of Applied Meteorology and Climatology*, *50*(10), 2167–2183. https://doi.org/10.1175/2011JAMC2689.1

Venkatesan, R., Mathiyarasu, R., & Somayaji, K. M. (2002). A study of atmospheric dispersion of radionuclides at a coastal site using a modified Gaussian model and a mesoscale sea breeze model. *Atmospheric Environment*, *36*, 2933–2942.